Hindawi
International Journal of Energy Research
Volume 2024, Article ID 5541306, 13 pages
https://doi.org/10.1155/2024/5541306

Research Article

Fabrication of Laser-Induced Graphene on Carbon Electrodes for Efficient Hydrogen Evolution Reaction

Md. Ali Asgar[1], **Chau Van Tran**[2], **Jun Kim**[2], **Chengjun Jin**[2], **Seongmin Lee**[2], **Young Kyu Kim**[2], **Xun Lu**[3], **Jung Bin In**[2] and **Seok-min Kim**[2]

[1]*Jatiya Kabi Kazi Nazrul Islam University, Mymensingh, Bangladesh*
[2]*Chung-Ang University, Seoul, Republic of Korea*
[3]*Yanbian University, Yanji, China*

Correspondence should be addressed to Jung Bin In; jbin@cau.ac.kr and Seok-min Kim; smkim@cau.ac.kr

Received 20 August 2023; Revised 13 January 2024; Accepted 15 March 2024; Published 29 April 2024

Academic Editor: Soumyendu Roy

Hierarchical porous carbon materials have received significant attention for application in catalytic water splitting because of their high efficiency, cost-effectiveness, and biocompatibility. In this study, laser-induced graphene (LIG) was fabricated on a carbon film- (CF-) type substrate for an efficient hydrogen evolution reaction (HER). The LIG-CF electrode was fabricated via laser-induced graphitization on a commercial polyimide (PI) film, followed by the pyrolysis of the LIG on the PI film (LIG-PI). During pyrolysis, the microscopic and material properties of the LIG remained intact, as verified through various characterizations. The as-prepared all-carbon electrode was then utilized as an electrode for the HER study in a 1.0 M KOH electrolyte and compared with LIG-PI and Pt electrodes. In the HER experiments, the optimized LIG-CF electrode exhibited excellent catalytic performance with zero-onset potential, and the potentials required to achieve high current densities of 10 and 20 mA/cm^2 were 134 and 139 mV (vs. reversible hydrogen electrode (RHE)), respectively. The excellent performance of the LIG-CF electrode originates from the hierarchical porous structure of the LIG material, which serves as an electrochemically active site, and carbon substrate that facilitates the fast transport of ions at the electrode/electrolyte interface. Additionally, the carbon substrate shortens the transportation length of electrons which played a significant role for the enhanced performance of the LIG-CF electrode.

1. Introduction

Hydrogen fuel has emerged as a promising and sustainable energy source that benefit the environment by decreasing the generation of greenhouse and other toxic gases. The hydrogen evolution reaction (HER) is at the pivot of water electrolysis [1]. However, HER from water electrolysis is a sluggish process, and catalysts are required to increase its efficiency in the long term. Thus far, noble metals (Pt, Ru, Ir, Pd, etc.) and their alloy-based catalysts have been developed, exhibiting the highest performance in electrocatalytic water electrolysis [2–6]. For instance, Li et al. prepared platinum (Pt) single-atom catalysts based on $Ni(OH)_x$ metal-organic framework (MOF) which require an overpotential of 58 mV to obtain a current density of 10 mA cm^{-2} [7]. Tang et al. reported heterostructure Mo_2C nanoparticle-Ru cluster-anchored carbon spheres (Mo_2C-Ru/C) which exhibited ultralow overpotential of 22 mV for obtaining identical current density [8]. However, their high cost and limited availability have impeded their application in industrial-scale hydrogen generation. Apart from precious metals, various earth-abundant transition metal (Cu, Fe, Ni, W, Mo, etc.)-based sulfides, phosphides, oxides, carbides, nitrides, etc., have also been demonstrated as cost-effective alternatives to noble metal catalysts for HER [9–18]. For example, Raja et al. synthesized nickel-molybdenum MOF-derived carbon-armored Ni_4Mo alloy catalysts which delivered a current density of 10 mA cm^{-2} at overpotential of 22 mV [19]. He et al. reported porous cobalt sulfide nanosheet arrays with copper incorporated supported on nickel foam (Cu-CoS_x/NF) via hydrothermal strategy assisted with sulfur vapor etching for water electrolysis. In the HER system, Cu-

CoS_x/NF represents excellent catalytic activity with the low overpotentials of 75 mV at 10 mA cm^{-2} [20]. However, their low selectivity, poor activity compared to noble metals, strong tendency toward gas poisoning, poor stability, and complex synthesis method of heterostructures have limited their industrial-scale acceptance [21, 22].

Recently, metal-free three-dimensional (3D) hierarchical porous carbon structures have emerged as potential candidates for electrocatalytic water splitting owing to their low cost, high efficiency, durability, high chemical resistance, and multifunctionality [23, 24]. Laser-induced graphene (LIG) is a carbon-based material primarily containing layered 3D porous graphene. LIG can be fabricated in a facile, scalable, and environmentally friendly manner through the laser-induced graphitization of engineering polymers, such as polyimide (PI), phenolic resins, and ligneous woods [25–28]. During the laser scanning of these pyrolysis precursors, the laser-induced heat breaks the C–O, C=O, and C–N chemical bonds at high temperatures, resulting in the rapid removal of gaseous contents and rearrangement of aromatic compounds to sp^2 carbon. Consequently, a LIG layer is generated on the nonconductive precursor substrate. Recently, LIG has received significant attention and has been utilized in various applications, including water splitting, because of its high specific surface area and good chemical stability [28, 29]. LIG's inherent 3D interconnected porous structure facilitates electrolyte/ion infiltration. Moreover, LIG contains numerous electrochemically active adsorption sites for hydrogen evolution reaction (HER), resulting in good HER performance. However, the overall electrical conductance of the LIG layer generated on a nonconductive substrate is limited because of the thin and porous graphene structure of LIG and the small thickness of the layer. Additionally, the electrons travel along the thin and porous LIG structure for reaching the electrical contact that increases the overall electron transfer length which subsequently can increase the resistance, resulting in deterioration of the HER performance.

For minimizing the electron transfer length in LIG (curtailing the resistance of electron transfer), the LIG structure on a conductive substrate has been proposed. For instance, Shim et al. fabricated LIG on PI substrate and transferred to a copper substrate by using the dry release transfer method [30]. Zhang et al. fabricated the LIG pattern on a copper foil by laser-induced graphitization of phenolic resin coated on a copper substrate [27]. Although the LIG on a metallic substrate enables highly efficient electron transfer, it might have some limitations when applied to water splitting because of relatively low chemical stability of metallic substrates and relatively high electron transfer energy barrier at the interface. Additionally, LIG can be delaminated at the interface due to harsh chemical environment of HER system [31].

In this study, we demonstrated a process of fabricating LIG film on a highly conductive carbon film (CF) and high electrochemical activity of this electrode in HER system. To fabricate LIG on the CF (LIG-CF) electrode, two simple steps were adopted: first, the LIG was fabricated on a PI film using an infrared CO_2 laser system, followed by the pyrolysis of the whole LIG on the PI film to obtain LIG on CF. The irradiated area of the PI film was converted into LIG via laser-induced graphitization during laser scanning. The PI material which was not affected by the laser irradiation entirely converted into CF via electric furnace pyrolysis. Since the initial PI substrate was converted into both LIG and CF, the length for electron transportation and delamination issue at the interface might be minimized. Additionally, the electrons generated in the electrochemical reaction can move smoothly through the LIG layer to the underlying CF substrate and hence to the external electrode. Consequently, the LIG-CF electrode exhibited fast electron transfer with negligible electrical contact resistance because carbon network could be generated between LIG and CF during the furnace pyrolysis process. Further, during furnace pyrolysis, a bulk shrinkage of PI substrate occurs resulting in delamination of the LIG film. To overcome the delamination problem, discrete LIG morphology on PI substrate was proposed by scanning the PI surface with modulated laser beam pulses at an optimized laser power. Finally, the HER performance of LIG-CF electrode was evaluated in an alkaline electrolyte and compared with those of the LIG-PI and state-of-the-art Pt electrodes.

2. Experimental Section

2.1. Fabrication of the LIG-CF Electrode. Figure 1 depicts the schematic for fabricating LIG on a CF substrate. Commercially available PI (Kapton HN PI film, thickness: 125 μm, McMaster-Carr, USA) was utilized as a precursor material for fabricating an LIG-CF electrode. PI is a carbon-rich imide group-containing polymer that can be converted into carbon upon heat treatment/pyrolysis [32, 33]. The PI film was used as received unless specified otherwise. First, the PI substrate was laser-induced graphitized using a CO_2 laser engraver system (C40–60, wavelength: 10.6 μm, Coryart, Republic of Korea) to fabricate LIG film. The scanning speed, diameter of laser beam spot, and raster scanning interval were selected as 200 mm/s, 260 μm, and 125 μm, respectively, based on our previous LIG fabrication experiments [34]. For achieving modulated laser beam pulses, a mechanical beam chopper (MC2000B-EC, Thorlabs, USA) with a chopper wheel (MC1F10HP, Thorlabs, USA) was used. The modulation frequency was set to 1 kHz, and the duty cycle of the beam chopper was 50%. To optimize the laser power for maximizing the HER performance of LIG on CF substrate, the laser power output was controlled from 5.4 to 11.4 W. The LIG obtained after the pulsed laser-induced graphitization of the PI film is denoted as LIG-PI-*x*, where *x* represents the laser power in watt. After the laser-induced graphitization of the PI film with different laser powers, the LIG-PI electrodes were cut into rectangular pieces (i.e., $20 \times 10\,mm^2$) as shown in Figures 2(h)–2(l). Additionally, as a control sample for comparison, we also fabricated LIG on PI at a laser power output of 5.4 W without using the chopper, and this sample is denoted by w/o-c-LIG-PI-5.4. The laser scanning area on the PI film was commonly $15 \times 10\,mm^2$ for all samples. Next, the pyrolysis of LIG-PI-x and w/o-c-LIG-PI-5.4 was performed using a

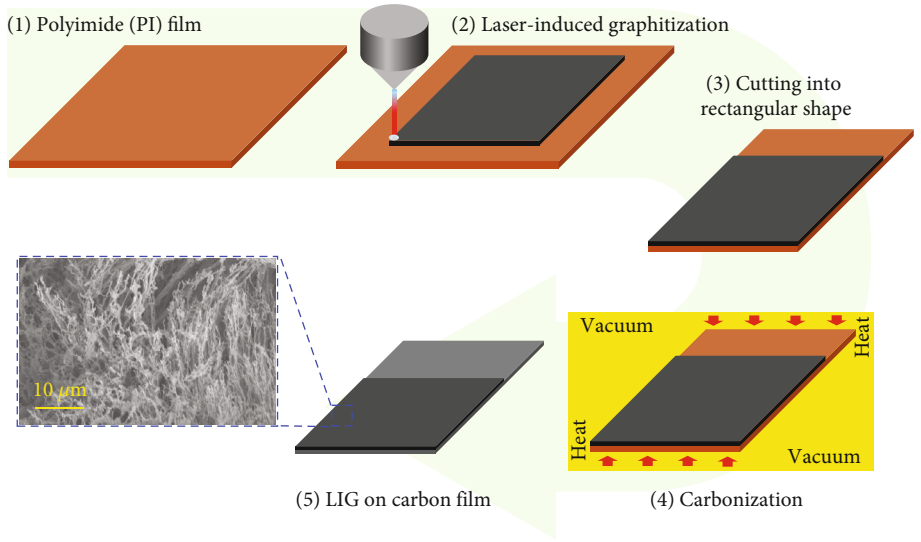

Figure 1: Schematic illustration of the fabrication process of laser-induced graphene (LIG) on carbon film-type substrate.

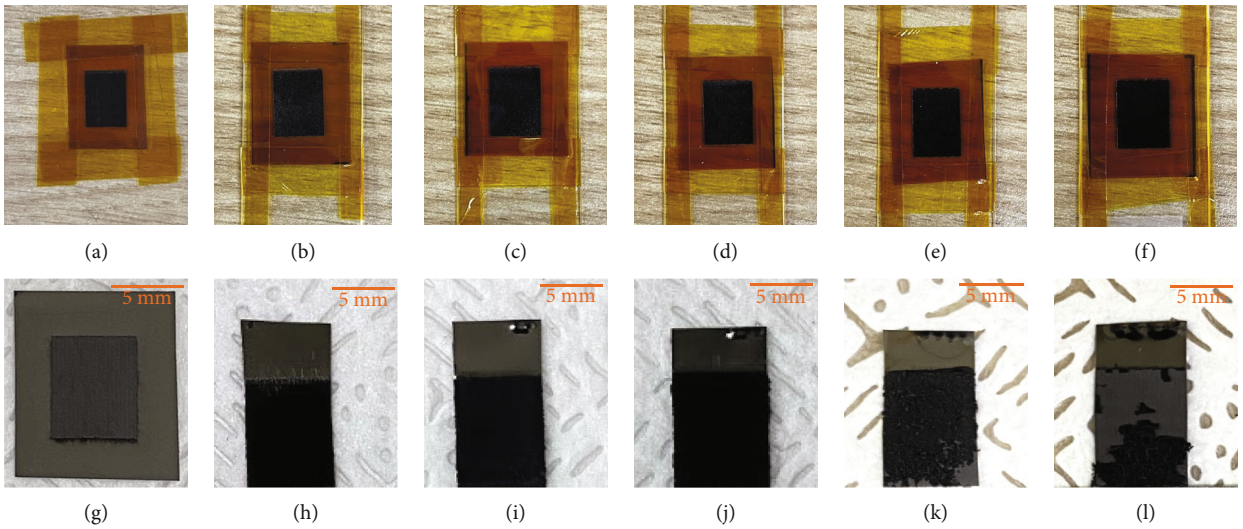

Figure 2: Laser-induced graphene (LIG) on (a) polyimide (PI) film and (g) carbon film fabricated without a chopper operation for a laser power of 5.4 W and (b–f) on a PI film and (h–l) carbon film (after pyrolysis) at laser powers of 5.4, 6.8, 8.2, 9.4, and 11.4 W fabricated with a chopper. Laser power was attenuated to 50 percent while patterning with chopper. Scale bar indicates the width of samples for LIG-CFs. Laser patterning areas on the PI film were identical ($10 \times 15\,\text{mm}^2$).

vacuum tube furnace (Mir tube furnace, Republic of Korea) to convert the remained PI film into CF. The vacuum pressure was maintained to approximately 1.0×10^{-3} torr during the pyrolysis process. The terminology CF was introduced because the thickness of the carbon substrate was nearly hundreds of microns after pyrolysis (Figure S1). Additionally, the as-fabricated samples were pyrolyzed together to obtain a consistent result. During pyrolysis, the furnace temperature was increased stepwise to 1000°C and maintained for 4 h at this temperature. The stepwise gradual increase of furnace temperature was optimized and reported in our previous experiment [35]. The LIG-CF electrode was obtained after natural cooling to room temperature, e.g., 25°C. During the thermal decomposition of polymer to carbon, different volatile gases were annealed out. A slow heating mechanism facilitated the steady removal of volatile gases. The LIG obtained after pyrolysis was denoted LIG-CF-*x*, where "*x*" represents the laser power in watt, for further analysis. A detailed description of the pyrolysis process in the electric furnace for polymer materials can be found in other literature and is not provided herein as the exploitation of LIG-CF electrodes in HER is the main focus of this study [36, 37].

2.2. Material Characterization. To identify the chemical structure of LIG on PI and CF substrates, Raman measurements were performed using a micro-Raman spectrometer (NOST, Republic of Korea) with an excitation laser

wavelength of 531 nm, laser power of 0.3 mW, and an objective lens with a 50x magnification. A wide wavenumber range from 969 to 3262 cm^{-1} was selected for the Raman measurements. The crystal structure of the LIG film was analyzed using field emission transmission electron microscopy (FE-TEM; JEOL, Japan) with an accelerating voltage of 200 kV. The LIG films were peeled off and sonicated in ethanol before being transferred to a CF200-CU carbon-copper TEM grid. Field emission scanning electron microscopy (FE-SEM; Carl Zeiss, USA) was used to study the surface morphology. For FE-SEM, images were taken from a working distance of 5 mm with an electron high tension (EHT) target voltage of 5 kV. A platinum coating was applied for 130 s with a current of 4 mA before performing the FE-SEM measurements of LIG-PI. The sheet resistance of LIG-PI-8.2 and LIG-CF-8.2 was measured using Keithley four-point probe meter (model: 2634B). To determine the elemental composition and perform quantitative analysis of LIG on the PI and CF films, X-ray photoelectron spectroscopy (XPS) (K-Alpha+, Thermo Fisher Scientific, USA) was performed using Al K-Alpha as an energy source for binding energies of 0–900 eV. For XPS measurements, the LIG films were peeled off from the PI and CF substrates, and measurement was carried out in powder form. XPS with LIG powder was adopted to investigate the average compositional characteristics as the LIG film produced by laser does not have uniform compositions along the depth on to the LIG-PI and LIG-CF electrodes. The analyzer mode was selected to utilize a pass energy of 200 eV for the survey scan and 40 eV for the high-resolution narrow-band spectra. The step sizes were adjusted to 0.1 and 1.0 eV for the high-resolution elemental spectra and survey scan, respectively. The XPS spectra were corrected using the C 1s peaks at 284.5 eV as reference.

2.3. Electrochemical Measurements. The electrochemical performance of the as-fabricated LIG-PI and LIG-CF electrodes toward the HER was evaluated using an electrochemical workstation (SP-150, Bio-Logic Science Instruments, USA) in three-electrode configuration. The HER activities were evaluated through linear sweep voltammetry (LSV) in the potential range of 0.20 to −0.40 (vs. RHE) at a scan rate of 5 mV/s in a standard three-electrode cell using 1.0 M KOH solution. The LSV scanning was performed after multiple activation cycles in the potential range of -1.0 to 1.0 V (vs. Hg/HgO (sat. 1.0 KOH)) at 20 mV/s (Figure S12). The reference and counter electrodes were Hg/HgO (sat. 1.0 M KOH) and Pt mesh, respectively. A polytetrafluoroethylene (PTFE) electrode holder (WizMAC Inc., Republic of Korea) was used to establish an interface between the electrolyte and working electrode. The LSV curves were iR-compensated using the potential equation of $E = E$ vs. $(\mathrm{RHE}) - iR_s$, where R_s is the electrolyte resistance, prior to obtaining the Tafel plots [38]. Electrochemical impedance spectroscopy (EIS) data were obtained in the frequency range of 100 mHz to 1.0 MHz at a sinusoidal amplitude of 10 mV. All potentials were converted to RHE using the equation $E(\mathrm{RHE}) = E/V$ vs. $\mathrm{Hg/HgO} + E^0(\mathrm{Ref}) + 0.059\,\mathrm{pH}$. The stability test of the highest-performing LIG-CF electrode was conducted by repeating the potential scan for 2000 cycles in the potential window of −0.80 to +0.20 V vs. Hg/HgO (sat. 1.0 M KOH) at a scan rate of 50 mV/s. Further, the chronoamperometry data were obtained in 1.0 M KOH for the long-term stability test of the LIG-CF-8.2 electrode at a fixed potential.

3. Results and Discussion

3.1. Surface Characteristics of LIG on the PI Substrate. FE-SEM was employed to study the surface morphology of LIG derived from the PI film. Figure 3 shows the top-view FE-SEM images of LIG on the PI substrate patterned by using the CO_2 laser for a laser power of 5.4 W, without a chopper (Figure 3(a)) and with a chopper for laser powers of 5.4, 6.8, 8.2, 9.4, and 11.4 W (Figures 3(b)–3(f)). The laser power reached to the sample surface was attenuated to 50% during laser machining using a chopper. Cross-sectional views of the FE-SEM images of LIG-PI are shown in Figure S2 and Figure S3. The low-magnification FE-SEM images revealed that a relatively uniform porous structure was produced when patterned without a chopper (Figure 3(a)). Zhang et al. and Khandelwal et al. reported identical 3D hierarchical porous morphology of LIG films on the PI substrate [29, 34]. However, discontinuous porous structures were generated when the chopper operation was introduced (Figures 3(b)–3(f)). Additionally, the high-magnification FE-SEM revealed highly porous nanofiber-like microstructures that were generated on laser-pyrolyzed regions for all LIG-PI samples (shown in insets). Interestingly, by adjusting the laser operational mode, LIG fiber (LIGF) can be produced for a critical laser fluence. Duy et al. reported the formation of LIGF by orienting laser in the vector mode with a critical laser fluence of 5.8 J cm^{-2} [39]. When a chopper was used, the laser-induced graphitized regions were well separated from the ungraphitized boundary regions. As expected, the width of the separation decreased with increasing laser power. A comparison of the ungraphitized region obtained with laser powers of 5.4 W and 11.4 W is shown in Figure S4. Notably, a highly porous morphology also appeared on the boundary regions with a higher laser power (Figure S4(f)), and the surface appeared quasicontinuous. Moreover, higher laser power tends to increase the porosity, as revealed by the cross-sectional FE-SEM measurements (Figure S3). The top and cross-sectional views revealed the production of numerous 3D interconnected porous LIG microstructures during laser patterning with or without a chopper, which provided numerous accessible active sites for electrolyte infiltration and electrocatalysis.

3.2. Effect of Chopper in the Furnace Pyrolysis. To convert the underlying PI substrate into a carbon substrate, the pyrolysis of the as-fabricated LIG-PI was performed in a vacuum environment. Figure 2 depicts real-view images of the samples before (Figures 2(a)–2(f)) and after pyrolysis (Figures 2(g)–2(l)). Figures 2(a) and 2(g)correspond to CO_2 laser patterning without a chopper, and Figures 2(b)–2(f) and 2(h)–2(l) correspond to CO_2 laser patterning with a chopper. When

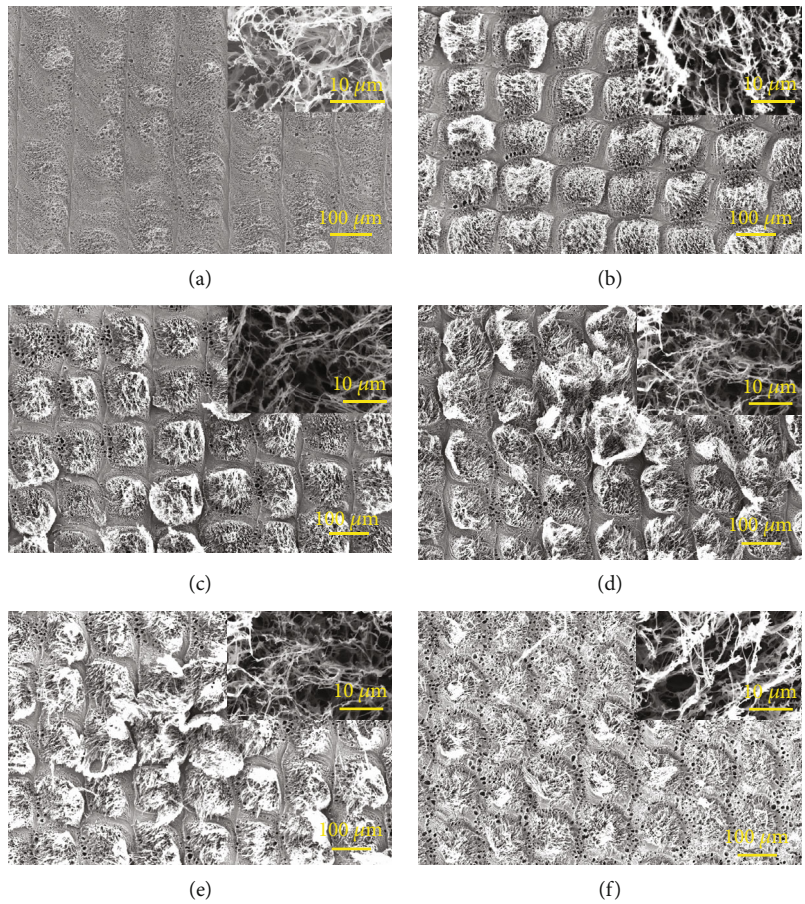

Figure 3: Top-view FE-SEM measurement of laser-induced graphene (LIG) on a polyimide (PI) film (a) without a chopper at a laser power of 5.4 W and (b–f) with a chopper at laser powers of 5.4, 6.8, 8.2, 9.4, and 11.4 W, respectively.

the PI substrate was patterned without a chopper, a relatively uniform porous structure was generated on the laser-patterned area of the PI substrate (Figure 3(a)). The stress developed during the thermal decomposition of the polymer to carbon can be considered as global stress. Consequently, the laser-induced graphitized parts, i.e., the LIG layer, was fully delaminated during pyrolysis. However, when the laser beam was modulated by introducing a chopper, certain areas of the PI substrate were laser-induced graphitized. Accordingly, laser-induced graphitization occurred only at specific locations. Therefore, the stress developed during furnace pyrolysis can be considered as local stress that results in the persistence of laser-induced graphitized parts on the substrate. However, when the laser power was very high, for, e.g., 11.4 W, the laser-induced graphitized regions started to coalesce. In other words, almost the entire area of the PI substrate was laser-induced graphitized during laser scanning. Consequently, the top surface appeared as a quasiuniform porous surface (Figure 3(f)). In some areas, the chopping region became nearly continuous, as revealed by the cross-sectional FE-SEM measurements (Figure S5). Therefore, the laser-induced graphitized parts started to delaminate at a laser power of 9.4 W (Figure 2(k)) and became fully delaminated with a laser power of 11.4 W (Figure 2(l)). Notably, no such delamination was observed, even at the microscopic level, with a laser power of 8.2 W (Figure S6). As partial delamination occurred on the laser-induced graphitized parts (LIG layers) with a laser power of 9.4 W during the furnace pyrolysis, the samples obtained with laser powers of 5.4, 6.8, and 8.2 W were used for further analysis.

3.3. Physiochemical Properties of LIG. Furthermore, the microstructure of LIG on both PI and CF substrates was investigated using FE-TEM. As displayed in Figures 4(a) and 4(b), flake-like few-layered features were observed on the surface of the LIG on the PI substrate obtained with a laser power of 8.2 W. High-resolution TEM measurements revealed the abundant presence of graphene fringes on the flake surfaces. The average lattice spacing between the graphene fringes was calculated to be 3.64 Å from the LIG on the PI substrate. The FE-TEM measurements obtained after pyrolysis at an identical laser power, i.e., at 8.2 W, shown in Figures 4(c) and 4(d), also revealed identical layered structures and graphene fringes. The average d-spacing between the graphene fringes was 3.68 Å after pyrolysis, which is very close to that of the LIG on the PI substrate. The presence of these graphene fringes enhances the performance of the electrode for electrocatalytic applications.

The chemical structures of LIG-PI and LIG-CF were investigated using micro-Raman spectroscopy. Figure 5(a) shows the Raman spectra of LIG-PI obtained at laser powers

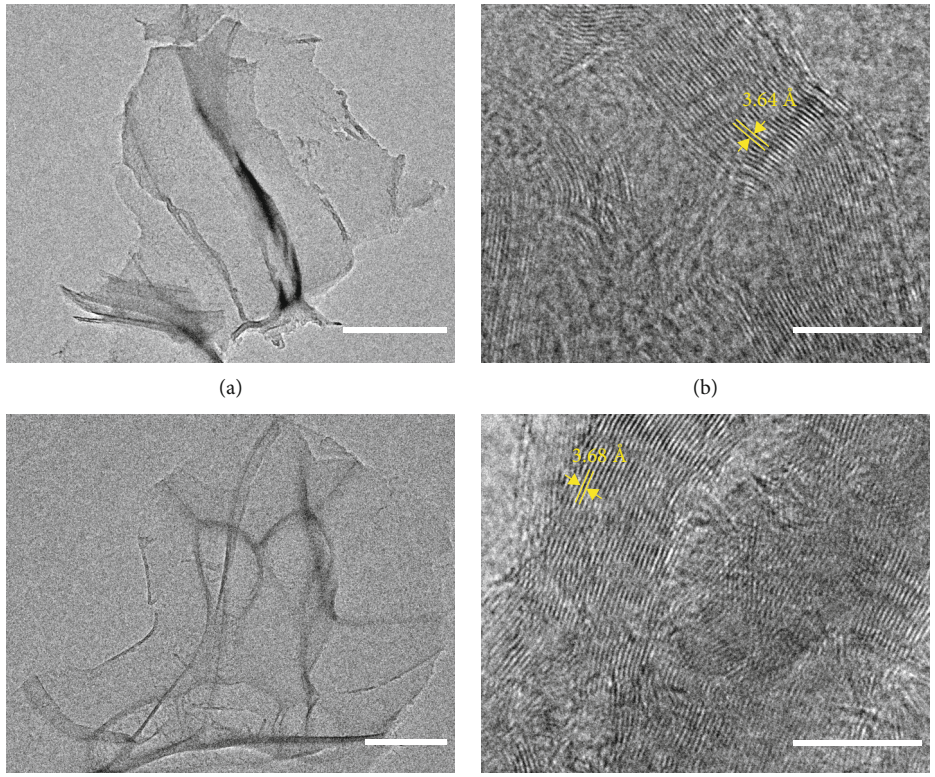

Figure 4: (a) Field emission transmission electron microscopy (FE-TEM) image of LIG-PI-8.2 and (b) high-resolution TEM (HRTEM) image of LIG-PI-8.2. (c) FE-TEM image of LIG-CF-8.2 and (b) HRTEM image of LIG-CF-8.2. Scale bars are (a, c) 1 μm and (b, d) 10 nm.

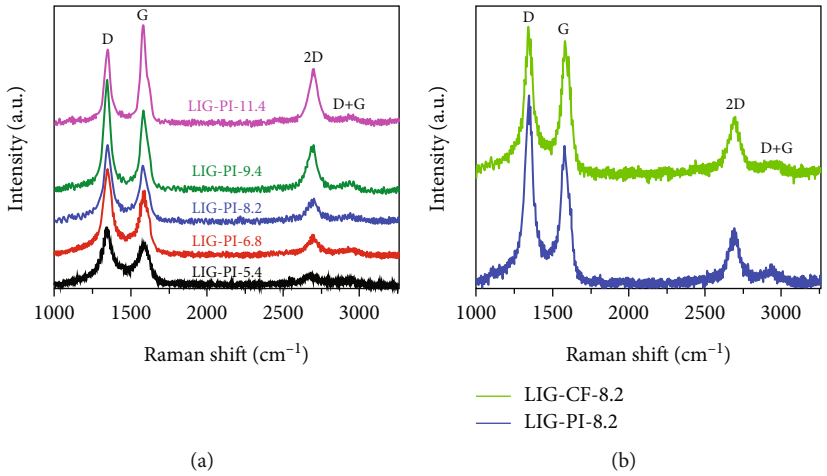

Figure 5: Raman spectra of (a) LIG-PI for laser powers of 5.4, 6.8, 8.2, 9.4, and 11.4 W and (b) comparison of Raman spectra of LIG-PI-8.2 and LIG-CF-8.2.

of 5.4, 6.8, 8.2, 9.4, and 11.4 W. The D, G, and 2D peaks were clearly observed at 1345, 1389, and 2700 cm^{-1}, respectively, for all laser powers. Moreover, the D and G peaks intensified with the increase in the laser power from 5.4 to 11.4 W, which demonstrates the formation of higher-quality graphene structures. Furthermore, the G and 2D peaks attained the highest intensity at a laser power of 11.4 W, indicating that a better-quality graphene structure than the others was formed. A Raman signature pattern was also obtained for w/o-c-LIG-PI-5.4, as shown in Figure S7(a). The graphene structure of LIG-PI was further analyzed using the D to G peak intensity (I_D/I_G) and 2D to G peak intensity (I_{2D}/I_G) ratios as summarized in Figure S8. Figure S8 demonstrates that defects on LIG structure increase with increasing the laser power and then decrease sharply at laser power of 11.4 W which signifies that quality

of graphene increased for laser power of 11.4 W. This indicates that when the laser power is 11.4 W, thermal power dominates the quality of the LIG films. Therefore, increased laser power leads to a higher degree of graphitization. Furthermore, a layered graphene structure was formed on the PI substrate when laser-induced graphitized with an infrared laser. The Raman spectroscopy of LIG was also performed after furnace pyrolysis using a sample obtained with a laser power of 8.2 W. The Raman signature pattern of the CF material is shown in Figure S7(b). The CF material was fabricated via the pyrolysis of an identical PI film, which was utilized for fabricating the LIG. As shown in Figure 5(b), identical D, G, and 2D peaks are observed for the LIG on the CF substrate with a laser power of 8.2 W (LIG-CF-8.2). Significantly, the Raman spectra revealed that the defects in the graphene structure were further reduced via furnace pyrolysis. Additionally, the I_D/I_G ratio decreased from 1.38 (LIG-PI-8.2) to 1.10, which may be due to further graphitization during furnace pyrolysis. Moreover, the layered graphene structure was maintained after pyrolysis, as confirmed by the I_{2D}/I_G ratio (Table S1). In contrast, the Raman spectra of the CF material (Figure S7(b)) are dissimilar to those of LIG and identical to those of amorphous carbon materials [40]. Therefore, the chemical structure of the LIG material remained almost identical during pyrolysis, whereas PI was converted into a carbon substrate. Moreover, the LIG material was stable up to the highest pyrolysis temperature of 1000°C in this study. Previously, Lin et al. reported that LIG was stable at approximately 900°C, using thermogravimetric analysis (TGA) [25].

To investigate the electrical properties of LIG-PI and LIG-CF, their sheet resistances were analyzed. The sheet resistance of LIG-PI-8.2 was measured and compared with that of LIG-CF-8.2. The sheet resistance was measured to be 12.18 and 0.072 Ω per square for LIG-PI-8.2 and LIG-CF-8.2, respectively. Lin et al. also found similar sheet resistance values for LIG on a PI substrate [25]. The sheet resistance of LIG-CF-8.2 was much lower than that of LIG-PI-8.2. During pyrolysis, the imide-containing polymer decomposed into a highly conductive carbon material, as revealed through sheet resistance measurements. Consequently, the sheet resistance of LIG-CF-8.2 was negligible compared with that of LIG-PI-8.2. A lower value of sheet resistance is highly desirable in electrocatalytic applications because it facilitates the fast transfer of electrons at the electrode-electrolyte interface.

Furthermore, to gain insight into the elemental composition and electronic state of LIG on the PI and CF substrates, XPS measurements were performed with the LIG samples that were prepared using a laser power of 8.2 W before and after pyrolysis. Figures 6(a) and 6(d) show the XPS survey scan of the LIG on both the PI and CF substrates. The survey scan results revealed that LIG on both the PI and CF substrates contained identical compositions and exhibited well-defined peaks corresponding to C 1s, O 1s, and N 1s. Duy et al. [39] and Khandelwal et al. [34] also observed identical compositions for LIG films in the similar binding energies. However, the most intense peaks were at the binding energies of 284.76 and 284.78 eV for LIG on PI and CF, respectively, which corresponded to C=C binding. The peaks at these binding energies indicate that a high degree of graphitization was mostly maintained in the LIG structure before and after furnace pyrolysis. The percentage of the elemental composition of LIG on PI and CF is summarized in Table S2. The XPS data revealed a negligible change in the elemental composition of LIG after pyrolysis. The narrow-band XPS spectrum of C 1s of LIG-PI can be further deconvoluted into three peaks at 284.6, 284.8, and 285.5 eV, which are ascribed to C=C, C–C, and C–O–C/C–N (Figure 6(b)). The high-resolution C 1s spectra of LIG-CF also revealed the presence of peaks associated with C=C (284.5 eV), C–C (284.8 eV), and C–O–C/C–N (285.6 eV), as shown in Figure 6(e). Notably, these peaks occurred at almost identical binding energies compared with those of the C 1s spectrum of LIG-PI. Furthermore, the N 1s spectrum of LIG-PI can be assigned to three nitrogen species: pyridinic (399.6 eV), pyrrolic (401.3 eV), and quaternary (402.9 eV) nitrogen (Figure 6(c)). Additionally, the high-resolution N 1s spectrum of LIG-CF revealed the existence of pyridinic (399.5 eV), pyrrolic (401.3 eV), and quaternary (402.9 eV) nitrogen (Figure 6(f)). The presence of nitrogen was also observed in the C 1s survey spectrum of the carbon functionalities. Moreover, these nitrogen functional groups further justify the appearance of surface defects, which subsequently increase the conductivity and number of active sites for ion adsorption in electrolytic media [41]. The deconvoluted O 1s spectra for both LIG-PI and LIG-CF are shown in Figure S9. The high-resolution O 1s spectra also indicate the presence of identical functionalities for LIG on PI and CF substrates. The presence of nitrogen and oxygen functionalities modifies the charge distribution of carbon atoms as electron acceptors because both N and O are negatively charged, which is beneficial for catalytic applications as they enhance charge transfer capacity. Furthermore, the deconvoluted C 1s, O 1s, and N 1s spectra for both LIG-PI and LIG-CF revealed negligible alterations in the LIG composition and functionalities after pyrolysis. The XPS results agree with the Raman and FE-TEM results and further confirm that the LIG structure was stable even at the highest pyrolysis temperature of 1000°C.

3.4. Electrochemical Characterization. The HER electrocatalytic activity of the as-fabricated LIG-PI and LIG-CF electrodes was evaluated using LSV in a 1.0 M KOH electrolyte in three-electrode configuration (Figure S10) and based on footprint geometrical area (Figure S11). Accordingly, the as-fabricated electrodes were directly used as the working electrode without requiring any device fabrication steps that provide flexibility and minimize cost which are beneficial for industrial application. Further, alkaline electrolyte usually provides less vapor pressure and lower corrosion of electrolytic cell and produces high purity hydrogen gas compared to acidic electrolyte [42]. For comparison, the performance of a state-of-the-art Pt electrode was measured under the same conditions. The performance of the CF

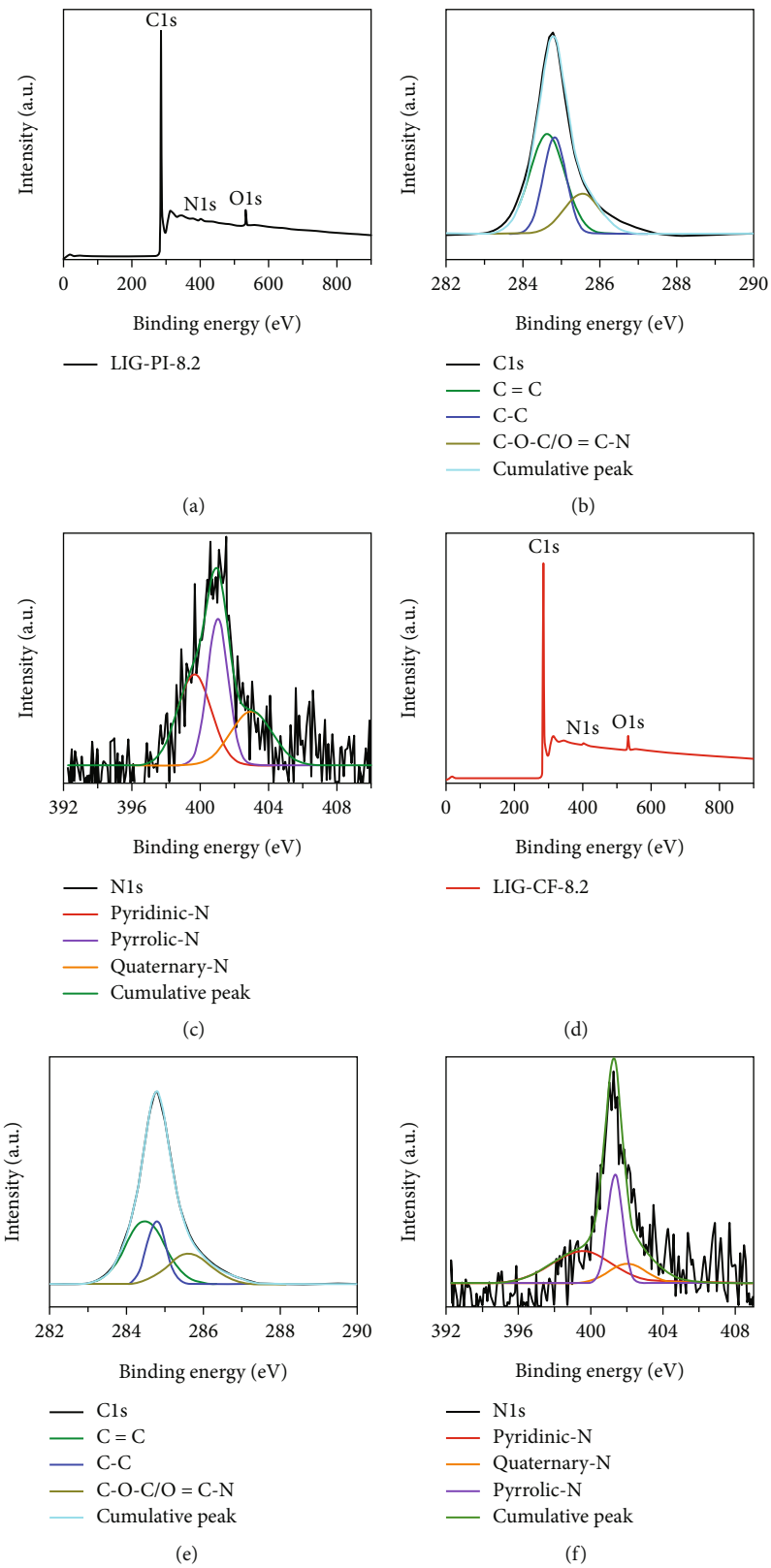

Figure 6: X-ray photoelectron spectroscopy (XPS) survey scan spectra of (a) LIG-PI-8.2 and (d) LIG-CF-8.2 for the binding energy from 0 to 900 eV. High-resolution deconvoluted images of (b, c) C 1s and N 1s of LIG-PI-8.2 and (e, f) C 1s and N 1s of LIG-CF-8.2, respectively.

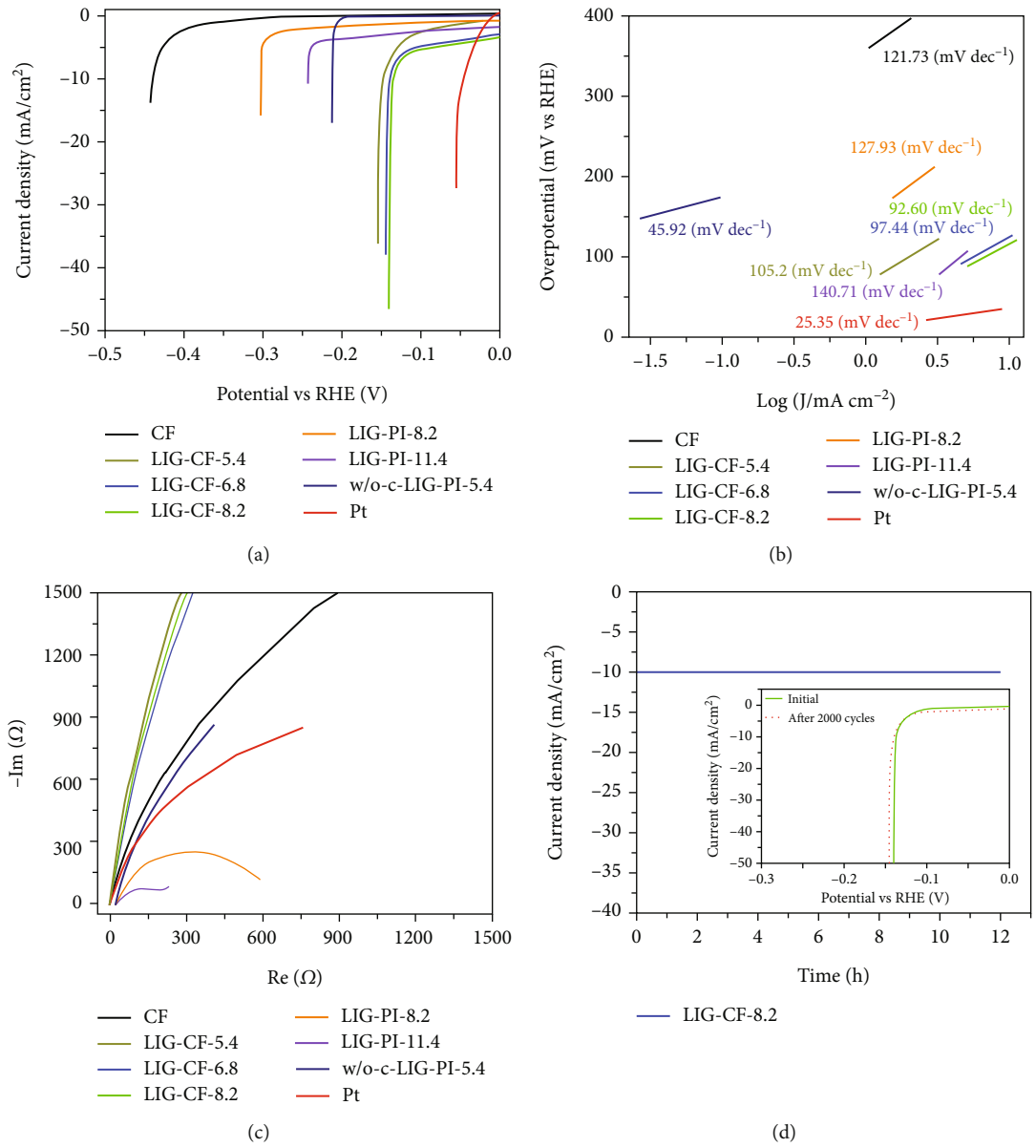

Figure 7: Hydrogen evolution reaction catalytic activities of CF, LIG-CFs, LIG-PIs, and Pt electrodes: (a) polarization curves, (b) Tafel plots, and (c) Nyquist plots for CF, LIG-CFs, LIG-PIs, and Pt electrodes and (d) stability analysis for LIG-CF-8.2.

electrode was also measured under the same test conditions because the LIG pattern was fabricated on a conductive carbon substrate. Figure 7 shows the HER catalytic activities of the CF, LIG-CF, LIG-PI, and Pt electrodes in a 1.0 M KOH obtained at a scan rate of 5 mV/s. Figure 7(a) reveals that Pt, LIG-CF, and LIG-PI electrodes exhibit zero-onset potential, except for CF. Significantly, LIG-CF-8.2 exhibited the lowest onset potential among the electrodes. The overpotentials required to achieve a cathodic current density of 10 mA/cm^2 were 45, 134, 138, 147, 242, 302, 212.2, and 440 mV for Pt, LIG-CF-8.2, LIG-CF-6.8, LIG-CF-5.4, LIG-PI-11.4, LIG-PI-8.2, w/o-c-LIG-PI-5.4, and CF, respectively. Additionally, a sharp increase of current density was observed for LIG-CF and LIG-PI electrodes which may be due to the high electrochemical surface area, and numerous active sites of LIG film. Furthermore, 3D hierarchical porous structure of LIG provides easy infiltration of electrolyte/ions to the active sites. A similar plummet on the LSV curves was also observed by Mugheri et al. and Xu et al. [43, 44]. As expected, the LIG-CF electrodes exhibited a significantly lower overpotential than the LIG-PI electrodes to obtain an identical current density. This was mainly because of the synergistic effect between the 3D hierarchical porous LIG structures and the highly conductive substrate. Owing to the synergistic effect, the transfer length of electrons may be shortened as LIG material was well connected with CF substrate. Furthermore, as the PI substrate was converted into CF via pyrolysis, no further processing was required for improving adhesion between LIG and CF, unlike other studies [45, 46]. The performance of LIG-CF-8.2 was comparable with those of other catalyst-loaded LIG material. For instance, Zhang et al. studied Pt-nanoparticle-

doped LIG and CoP-electrodeposited LIG structures on PI substrates for HER, and the overpotential required to obtain the identical current density was 110 mV RHE and 114 mV (vs. RHE) for Pt-doped LIG and CoP-electrodeposited LIG, respectively [29]. Ye et al. demonstrated CoP-electrodeposited LIG synthesized from pine wood for water splitting, and the optimized structure requires an overpotential of 130 mV for obtaining the current density of 10 mA/cm^2 [28]. Furthermore, the performance of LIG-CF-8.2 electrode is compared with that of carbon-based materials and is represented in Table S3.

To investigate the probable mechanism of hydrogen evolution on the electrode surface, the slope of the Tafel plot was examined. An active electrocatalyst generally exhibits a low Tafel slope and high current density, resulting in rapid hydrogen evolution with an applied overpotential. In addition, depending on the physiochemical and electronic properties of the electrode surface, the reaction kinetics can be explained using either the Volmer–Tafel or Volmer–Heyrovsky mechanism [47, 48]. Figure 7(b) shows the Tafel curves for the Pt, LIG-CF-8.2, LIG-CF-6.8, LIG-CF-5.4, LIG-PI-11.4, LIG-PI-8.2, w/o-c-LIG-PI-5.4, and CF electrodes. As expected, the lowest Tafel slope, 25.35 mV dec^{-1}, was obtained for the Pt catalyst, indicating the fastest HER kinetics. Moreover, the electrochemical reaction kinetics on the Pt electrode followed the Volmer–Tafel pathway and were consistent with that of the known HER system on Pt electrodes [49]. In contrast, the Tafel slopes for LIG-CF-8.2, LIG-CF-6.8, LIG-CF-5.4, LIG-PI-11.4, LIG-PI-8.2, w/o-c-LIG-PI-5.4, and CF were 92.60, 97.44, 105.20, 140.71, 127.93, 45.92, and 121.73 mV dec^{-1}, respectively. Significantly, the lower Tafel slopes were also observed on LIG-CF electrodes compared with LIG-PI electrodes; in particular, the representative LIG-CF-8.2 electrode showed the lowest Tafel slope (92.60 mV dec^{-1}), and the reaction pathways followed the Volmer–Heyrovsky method. Note that the higher Tafel slopes of LIG-CF-6.8, LIG-CF-5.4, LIG-PI-8.2, and LIG-PI-11.4 are also consistent with their relatively inferior catalytic activities in the HER kinetics.

EIS measurements were performed to investigate the HER kinetics at the electrode-electrolyte interface. The Nyquist plots for the Pt, LIG-CF-8.2, LIG-CF-6.8, LIG-CF-5.4, LIG-PI-11.4, LIG-PI-8.2, w/o-c-LIG-PI-5.4, and CF electrodes are shown in Figure 7(c). Further, the fitting model for the Nyquist plots for as-characterized electrodes are summarized in supplementary material Figure S13 and Figure S14. The high-frequency region of the Nyquist plot is shown in Figure S15. Both the high-frequency region corresponding to hydrogen adsorption and low-frequency region indicating HER kinetics were observed for all electrode materials. Importantly, the Nyquist plots of Pt, LIG-CF, CF, and w/o-c-LIG-PI-5.4 were vertical over the long frequency range from 100 mHz to 1.0 MHz. Moreover, no semicircular sections were observed in the high-frequency region, which indicates the fast transfer rate of ions [34]. In contrast, LIG-PI-8.2 and LIG-PI-11.4 exhibited semicircular Nyquist plots for the identical frequency region, particularly LIG-PI-11.4, which demonstrated a smaller semicircle radius than LIG-PI-8.2. The vertical lines of the LIG-CF electrodes further suggest the fast transfer rate of ions in the HER kinetics. Furthermore, equivalent series resistance (ESR) data were retrieved from the Nyquist plots in the high-frequency region, and the ESR data reveal that LIG-CF has a lower ESR value than that of LIG-PI (particularly, LIG-CF-8.2 (4.28 Ω), LIG-CF-6.8 (4.15 Ω), LIG-CF-5.4 (4.35 Ω), LIG-PI-11.4 (39.07 Ω), LIG-PI-8.2 (36.33 Ω), and w/o-c-LIG-PI-5.4 (16.35 Ω). A lower equivalent series resistance corresponds to faster kinetics of electrocatalysts; therefore, a lower ESR represents a faster transfer of ions/charges at the electrode-electrolyte interface in the HER system. The EIS measurements further agree with the equivalent series resistance measurements (Figure S15) and the polarization curve analysis Figure 7(a). The electrochemical performance of as-fabricated samples is summarized in supplementary material Table S4.

Catalyst stability is another crucial complementary parameter for developing industrially applicable catalysts for HER systems. Pyrolytic porous carbon is commonly used for various energy storage applications owing to its mechanical stability and stable electrocatalytic characteristics in alkaline electrolytes [50, 51]. The stability analysis of the LIG-CF-8.2 electrode was accomplished by performing constant cyclic voltammetry (CV) for 2000 cycles and current-time response for 12 h at a fixed potential of 134 mV vs. RHE in an identical electrolyte. Cyclic stability and current-time/potential-time responses are commonly employed for stability analysis in HER system [52]. The performance of the LIG-CF-8.2 electrode was measured and compared with its initial performance in cyclic stability test. Figure 7(d) illustrates the durability analysis of the LIG-CF-8.2 electrode. The decrease in catalytic activity is hardly observed after 12 h chronoamperometry (CA) test and 2000 long cycles. Additionally, surface morphology study using FESEM before and after the stability test represents negligible delamination of LIG from substrate (Figure S16). These results imply that the LIG-CF-8.2 electrocatalyst exhibits high stability for catalytic water electrolysis in alkaline electrolyte.

4. Conclusions

In summary, a method to fabricate LIG on CF-type substrates was demonstrated. To fabricate LIG on the CF substrate, laser patterning on PI followed by the pyrolysis of LIG-PI was performed. During pyrolysis, the conversion of the PI substrate to the carbon substrate occurred. In polymer-to-carbon conversion, unavoidable shrinkage occurs when polymer materials pass through a semisolid phase. This shrinkage causes the peeling of LIG from the substrate. However, this problem was overcome by the introduction of a chopper operation during laser patterning on the PI substrate. The microstructure and material properties of the LIG remained almost intact during the conversion of nonconductive PI to highly conductive carbon. Additionally, the sheet resistance of LIG-CF was considerably lower than that of LIG-PI. Finally, the as-fabricated LIG-CF electrode was utilized for a catalytic HER study, and it exhibited high efficiency in alkaline water splitting. The LIG-CF

electrode exhibited zero-onset potential, and the best-performing electrode exhibited an overpotential of 134 mV for a current density of 10 mA/cm^2. The excellent performance of the LIG-CF electrode is superior to LIG-PI electrode and comparable to active material-loaded LIG electrodes. In LIG-CF, the interconnected porous LIG facilitates efficient electrolyte infiltration, and the conductive CF facilitates in shortening the electron transfer length. Consequently, the synergistic action of LIG and CF enhances the performance of the HER system. Therefore, considering the superior performance of the LIG-CF electrode obtained using a low-cost fabrication approach compared with the performance of the others LIG-PI, we believe that the LIG-CF electrode is a potential candidate for industrial-scale HER applications. The deposition of active catalysts onto LIG on carbon substrate is our ongoing research for further enhancement of HER performance.

Data Availability

The data used to support the findings of this study are included within the article.

Conflicts of Interest

The authors declare that there is no conflict of interest regarding the publication of this paper.

Authors' Contributions

Conceptualization and design of experiments were contributed by S.-M. Kim and J.B. In. Laser scanning was contributed by C.V. Tran and M.A. Asgar. Measurement and analysis of structural and chemical properties were carried out by M.A. Asgar, J. Kim, C. Jin, S. Lee, Y.K. Kim, and X. Lu. EC measurements were assisted by M.A. Asgar and C.V. Tran. Data analysis and writing were carried out by M.A. Asgar, X. Lu, S.-M. Kim, and J.B. In. All authors have read and approved the final version of the manuscript. Jung Bin In and Seok-min Kim contributed equally to this work.

Acknowledgments

This work was supported by the National Research Foundation of Korea (NRF) grant funded by the Korea government (MSIT) (No. 2021R1A2C2004458 and No. NRF-2022R1A2C1010296).

Supplementary Materials

Separate supplementary material file is provided to show detail experimental results of this paper. The supplementary material file includes the following. Figure S1: the thickness of (a) polyimide (PI) film (before pyrolysis) and (b) carbon film (CF) (after pyrolysis). Figure S2: (a) low- and (b) high-magnification cross-sectional FE-SEM measurement of laser-induced graphene (LIG) on polyimide film with laser power of 5.4 W. Relatively continuous LIG was found when no chopper operation was used. Figure S3: low- and high-magnification cross-sectional FE-SEM measurement of laser-induced graphene (LIG) on polyimide film with laser power of (a, b) 5.4 W, (c, d) 6.8 W, (e, f) 8.2 W (g, h) 9.4 W, and (i, j) 11.4 W with a chopper. Lower laser powers are tended to produce holey LIG (b, d, f), and higher laser powers are inclined to produce LIG fiber (h, j). Figure S4: low- and high-magnification FE-SEM measurement of laser-induced graphene (LIG) on polyimide film with laser power of (a–c) 5.4 W and (d–f) 11.4 W with chopper. Figure S5: low- and high-magnification FESEM measurements of LIG-PI fabricated with laser power of 11.4 W, showing nearly continuous LIG with chopper on PI substrate. Figure S6: low- and high-magnification cross-sectional FESEM of LIG on carbon film, after pyrolysis, fabricated with laser power of 8.2 W. Figure S7: the Raman spectral data of (a) w/o-c-LIG-PI-5.4 and (b) CF. The Raman spectra of LIG on PI substrate fabricated with laser power of 5.4 W without chopper has identical spectrum signature with LIG fabricated with chopper as illustrated in Figure 5(a). The Raman spectra of CF is dissimilar to LIG (absence of 2D peak) material and identical with amorphous carbon materials. Figure S8: (a) I_D and I_G ratio and (b) I_{2D} and I_G ratio of LIG on PI substrate obtained from the Raman signature. The graph illustrates that the graphene quality increases with the increase of laser power and multilayer graphene structure has been formed during laser patterning with chopper. Additionally, the I_{2D}/I_G ratio indicates that multilayer graphene structure has been developed while laser machining with a chopper. Figure S9: the high-resolution spectra of O1 s. (a) LIG-PI-8.2 and (b) LIG-CF-8.2. The deconvoluted spectra showed no difference in functional groups present in LIG material on PI and CF substrates. Figure S10: the three-electrode setup. (a) Schematics and (b) a photograph of the electrolytic cell. Plenty of hydrogen (H_2) bubbles had been observed on the working electrode during the electrocatalytic process (b). Figure S11: the original view of LIG on carbon film (CF) and LIG-CF working electrode. The geometrical area of LIG film was 12×8 mm^2 on the CF substrate. Figure S12: the multiple activation cycles for LIG-CF-8.2 electrode in 1.0 M KOH electrolyte prior to take the linear sweep voltammetry (LSV) scanning. The cyclic voltammetry (CV) scanning was performed in the potential range of -1.0 to 1.0 V (vs. Hg/HgO (sat. 1.0 KOH)) at 20 mV/s. Figure S13: the fitting model for the Nyquist plots with corresponding Randles circuits for (a) CF, (b) LIG-CF-5.4, (c) LIG-CF-6.8, and (d) LIG-CF-8.2 electrodes. Figure S14: the fitting model for the Nyquist plots with corresponding Randles circuits for (a) LIG-PI-8.2, (b) LIG-PI-11.4, (c) w/o-cLIG-PI-5.4, and (d) Pt electrodes. Figure S15: the high-frequency region of Nyquist plot of (a) CF, LIG-CFs, and Pt, and (b) LIG-PI electrodes. Figure S16: the FESEM study (a) before stability test and (b) after stability test of LIG-CF-8.2 electrode. Table S1: the Raman spectral data of LIG-PI-8.2 and LIG-CF-8.2 fabricated with laser power of 8.2 W. Table S2: the elemental composition of carbon, oxygen, and nitrogen in LIG-PI-8.2 and LIG-CF-8.2 for an identical laser power of 8.2 W. Table S3: the comparison of the HER performance of carbon-based materials. Acronyms: N: nitrogen; P: phosphorous; S: sulfur; CNT: carbon nanotube; PDA: polydopamine;

Mo: molybdenum; Co: cobalt; C: carbon; MoNiNC: molybdenum-nickel bimetallic carbonitride; MoC-MoP/BCNC NFs: MoC-MoP nanoparticles supported by bacterial cellulose-derived N-doped carbon nanofibers; VN/Co@NCNT: Co-encapsulated N-doped carbon nanotubes; Ni-NCNT: nickel nanoparticle on N-doped CNT; NiFe-LDH: NiFe-layer double hydroxide; MCF: microporous carbon framework; LIG-CF: laser-induced graphene on carbon film; N/A: not available. Table S4: the summary of fabrication condition (laser power) and results obtained in 1.0 M KOH electrolyte of as-fabricated electrodes. Acronyms: Pt: platinum; CF: carbon film; w/o-c-LIG-PI: without chopper continuous laser-induced graphene on polyimide; LIG-PI: laser-induced graphene on polyimide; LIG-CF: laser-induced graphene on carbon film; N/A: not available. *(Supplementary Materials)*

References

[1] P. F. Liu, H. Yin, H. Q. Fu, M. Y. Zu, H. G. Yang, and H. Zhao, "Activation strategies of water-splitting electrocatalysts," *Journal of Materials Chemistry A*, vol. 8, no. 20, pp. 10096–10129, 2020.

[2] Y. Chen, R. Ding, J. Li, and J. Liu, "Highly active atomically dispersed platinum-based electrocatalyst for hydrogen evolution reaction achieved by defect anchoring strategy," *Applied Catalysis B: Environmental*, vol. 301, article 120830, 2022.

[3] H. Miao, D. Zhang, Y. Shi et al., "Ultrasmall noble metal doped Ru2P@Ru/CNT as high-performance hydrogen evolution catalysts," *ACS Sustainable Chemistry & Engineering*, vol. 9, no. 44, pp. 15063–15071, 2021.

[4] H. Jin, S. Sultan, M. Ha, J. N. Tiwari, M. G. Kim, and K. S. Kim, "Simple and scalable mechanochemical synthesis of noble metal catalysts with single atoms toward highly efficient hydrogen evolution," *Advanced Functional Materials*, vol. 30, no. 25, article 2000531, 2020.

[5] F. Gao, Y. Zhang, Z. Wu, H. You, and Y. Du, "Universal strategies to multi-dimensional noble-metal-based catalysts for electrocatalysis," *Coordination Chemistry Reviews*, vol. 436, article 213825, 2021.

[6] D. K. K. Kori, R. G. Jadhav, L. Dhruv, and A. K. Das, "A platinum nanoparticle doped self-assembled peptide bolaamphiphile hydrogel as an efficient electrocatalyst for the hydrogen evolution reaction," *Nanoscale Advances*, vol. 3, no. 23, pp. 6678–6688, 2021.

[7] Q. Li, Q. Zhang, W. Xu et al., "Sowing single atom seeds: a versatile strategy for hyper-low noble metal loading to boost hydrogen evolution reaction," *Advanced Energy Materials*, vol. 13, no. 10, article 2203955, 2023.

[8] R. Tang, Y. Yang, Y. Zhou, and X. Y. Yu, "Rational design of heterostructured Ru cluster-based catalyst for pH universal hydrogen evolution reaction and high-performance Zn-H_2O battery," *Advanced Functional Materials*, vol. 34, no. 5, article 2301925, 2024.

[9] F. Keivanimehr, S. Habibzadeh, A. Baghban et al., "Electrocatalytic hydrogen evolution on the noble metal-free MoS_2/carbon nanotube heterostructure: a theoretical study," *Scientific Reports*, vol. 11, no. 1, p. 3958, 2021.

[10] Z. Ge, B. Fu, J. Zhao, X. Li, B. Ma, and Y. Chen, "A review of the electrocatalysts on hydrogen evolution reaction with an emphasis on Fe, Co and Ni-based phosphides," *Journal of Materials Science*, vol. 55, no. 29, pp. 14081–14104, 2020.

[11] C. Wang, Y. Li, C. Gu, L. Zhang, X. Wang, and J. Tu, "Active Co@CoO core/shell nanowire arrays as efficient electrocatalysts for hydrogen evolution reaction," *Chemical Engineering Journal*, vol. 429, article 132226, 2022.

[12] D. Reynard, B. Nagar, and H. Girault, "Photonic flash synthesis of Mo_2C/graphene electrocatalyst for the hydrogen evolution reaction," *ACS Catalysis*, vol. 11, no. 9, pp. 5865–5872, 2021.

[13] C. Wang, Y. Li, X. Wang, and J. Tu, "N-doped NiO nanosheet arrays as efficient electrocatalysts for hydrogen evolution reaction," *Journal of Electronic Materials*, vol. 50, no. 9, pp. 5072–5080, 2021.

[14] Z. Chen, X. Liu, P. Xin et al., "Interface engineering of NiS@-MoS_2 core-shell microspheres as an efficient catalyst for hydrogen evolution reaction in both acidic and alkaline medium," *Journal of Alloys and Compounds*, vol. 853, article 157352, 2021.

[15] T. Fujimura, M. Kunimoto, Y. Fukunaka, and T. Homma, "Analysis of the hydrogen evolution reaction at Ni micropatterned electrodes," *Electrochimica Acta*, vol. 368, article 137678, 2021.

[16] A. Elgendy, A. A. Papaderakis, C. Byrne et al., "Nanoscale Chevrel-phase Mo_6S_8 prepared by a molecular precursor approach for highly efficient electrocatalysis of the hydrogen evolution reaction in acidic media," *ACS Applied Energy Materials*, vol. 4, no. 11, pp. 13015–13026, 2021.

[17] N. Dubouis, C. Yang, R. Beer, L. Ries, D. Voiry, and A. Grimaud, "Interfacial interactions as an electrochemical tool to understand Mo-based catalysts for the hydrogen evolution reaction," *ACS Catalysis*, vol. 8, no. 2, pp. 828–836, 2018.

[18] A. T. A. Ahmed, A. S. Ansari, S. M. Pawar, B. Shong, H. Kim, and H. Im, "Anti–corrosive FeO decorated $CuCo_2S_4$ as an efficient and durable electrocatalyst for hydrogen evolution reaction," *Applied Surface Science*, vol. 539, article 148229, 2021.

[19] D. S. Raja, C. C. Cheng, Y. C. Ting, and S. Y. Lu, "NiMo-MOF-derived carbon-armored Ni4Mo alloy of an interwoven nanosheet structure as an outstanding pH-universal catalyst for hydrogen evolution reaction at high current densities," *ACS Applied Materials & Interfaces*, vol. 15, pp. 20130–20140, 2023.

[20] H. He, L. Zeng, X. Peng et al., "Porous cobalt sulfide nanosheets arrays with low valence copper incorporated for boosting alkaline hydrogen evolution via lattice engineering," *Chemical Engineering Journal*, vol. 451, article 138628, 2023.

[21] Q. Wang, R. Guo, Z. Wang et al., "Progress in carbon-based electrocatalyst derived from biomass for the hydrogen evolution reaction," *Fuel*, vol. 293, article 120440, 2021.

[22] J. Wang, H. Kong, J. Zhang, Y. Hao, Z. Shao, and F. Ciucci, "Carbon-based electrocatalysts for sustainable energy applications," *Progress in Materials Science*, vol. 116, article 100717, 2021.

[23] Y. Lv, B. Kang, Y. Yuan, G. Chen, and J. Y. Lee, "Activating γ-graphyne nanoribbons as bifunctional electrocatalysts toward oxygen reduction and hydrogen evolution reactions by edge termination and nitrogen doping," *Chemical Engineering Journal*, vol. 430, article 133126, 2022.

[24] D. V. Jawale, F. Fossard, F. Miserque et al., "Carbon nanotube-polyoxometalate nanohybrids as efficient electro-catalysts for the hydrogen evolution reaction," *Carbon*, vol. 188, pp. 523–532, 2022.

[25] J. Lin, Z. Peng, Y. Liu et al., "Laser-induced porous graphene films from commercial polymers," *Nature Communications*, vol. 5, no. 1, p. 5714, 2014.

[26] A. Lamberti, M. Serrapede, G. Ferraro et al., "All-SPEEK flexible supercapacitor exploiting laser-induced graphenization," *2D Materials*, vol. 4, no. 3, article 035012, 2017.

[27] Z. Zhang, M. Song, J. Hao, K. Wu, C. Li, and C. Hu, "Visible light laser-induced graphene from phenolic resin: a new approach for directly writing graphene-based electrochemical devices on various substrates," *Carbon*, vol. 127, pp. 287–296, 2018.

[28] R. Ye, Y. Chyan, J. Zhang et al., "Laser-induced graphene formation on wood," *Advanced Materials*, vol. 29, no. 37, pp. 1–7, 2017.

[29] J. Zhang, C. Zhang, J. Sha, H. Fei, Y. Li, and J. M. Tour, "Efficient water-splitting electrodes based on laser-induced graphene," *ACS Applied Materials & Interfaces*, vol. 9, no. 32, pp. 26840–26847, 2017.

[30] H. C. Shim, C. V. Tran, S. Hyun, and J. B. In, "Three-dimensional laser-induced holey graphene and its dry release transfer onto Cu foil for high-rate energy storage in lithium-ion batteries," *Applied Surface Science*, vol. 564, article 150416, 2021.

[31] D. V. Lopes, N. F. Santos, J. P. Moura, A. J. S. Fernandes, F. M. Costa, and A. V. Kovalevsky, "Design of laser-induced graphene electrodes for water splitting," *International Journal of Hydrogen Energy*, vol. 48, no. 11, pp. 4158–4172, 2023.

[32] S. Zhao, Z. Shi, C. Wang, and M. Chen, "Structure and surface elemental state analysis of polyimide resin film after carbonization and graphitization," *Journal of Applied Polymer Science*, vol. 108, no. 3, pp. 1852–1856, 2008.

[33] M. Schumann, R. Sauerbrey, and M. C. Smayling, "Permanent increase of the electrical conductivity of polymers induced by ultraviolet laser radiation," *Applied Physics Letters*, vol. 58, no. 4, pp. 428–430, 1991.

[34] M. Khandelwal, C. V. Tran, and J. B. In, "Nitrogen and phosphorous Co-doped laser-induced graphene: a high-performance electrode material for supercapacitor applications," *Applied Surface Science*, vol. 576, article 151714, Part A, 2022.

[35] M. A. Asgar, J. Kim, S. Lee et al., "Fabrication of 3D-interconnected microporous carbon decorated with microspheres for highly efficient hydrogen evolution reactions," *Microchemical Journal*, vol. 189, article 108571, 2023.

[36] M. A. Asgar, J. Kim, J. W. Yeom, S. Lee, M. R. Haq, and S. Kim, "Facile fabrication of microporous vitreous carbon for oil/organic solvent absorption," *Environmental Technology and Innovation*, vol. 24, article 101946, 2021.

[37] M. R. Haq, J. Kim, J. W. Yeom et al., "Fabrication of Cross-Sinusoidal Anti-Reflection Nanostructure on a glass substrate using imperfect glass imprinting with a nano-pin array vitreous carbon stamp," *Micromachines*, vol. 11, no. 2, p. 136, 2020.

[38] S. Anantharaj and S. Noda, "*iR* drop correction in electrocatalysis: everything one needs to know!," *Journal of Materials Chemistry A*, vol. 10, no. 17, pp. 9348–9354, 2022.

[39] L. X. Duy, Z. Peng, Y. Li, J. Zhang, Y. Ji, and J. M. Tour, "Laser-induced graphene fibers," *Carbon*, vol. 126, pp. 472–479, 2018.

[40] S. K. Ramasahayam, U. B. Nasini, V. Bairi, A. U. Shaikh, and T. Viswanathan, "Microwave assisted synthesis and characterization of silicon and phosphorous co-doped carbon as an electrocatalyst for oxygen reduction reaction," *RSC Advances*, vol. 4, no. 12, pp. 6306–6313, 2014.

[41] Y. Li, C. Ai, S. Deng et al., "Nitrogen doped vertical graphene as metal-free electrocatalyst for hydrogen evolution reaction," *Materials Research Bulletin*, vol. 134, article 111094, 2021.

[42] N. Mahmood, Y. Yao, J. W. Zhang, L. Pan, X. Zhang, and J. J. Zou, "Electrocatalysts for hydrogen evolution in alkaline electrolytes: mechanisms, challenges, and prospective solutions," *Advanced Science*, vol. 5, no. 2, article 1700464, 2018.

[43] A. Q. Mugheri, A. A. Otho, and A. A. Mugheri, "Meritorious spatially on hierarchically Co_3O_4/MoS_2 phase nanocomposite synergistically a high-efficient electrocatalyst for hydrogen evolution reaction performance: recent advances & future perspectives," *International Journal of Hydrogen Energy*, vol. 46, no. 44, pp. 22707–22718, 2021.

[44] K. Xu, F. Wang, Z. Wang et al., "Component-controllable $WS_{2(1-x)}Se_{2x}$ Nanotubes for efficient hydrogen evolution reaction," *ACS Nano*, vol. 8, no. 8, pp. 8468–8476, 2014.

[45] D. N. Sangeetha and M. Selvakumar, "Active-defective activated carbon/MoS_2 composites for supercapacitor and hydrogen evolution reactions," *Applied Surface Science*, vol. 453, pp. 132–140, 2018.

[46] D. Ko, X. Jin, K. D. Seong et al., "Few-layered MoS_2 vertically aligned on 3D interconnected porous carbon nanosheets for hydrogen evolution," *Applied Catalysis B: Environmental*, vol. 248, pp. 357–365, 2019.

[47] Y. N. Zhou, Y. R. Zhu, X. Y. Chen, B. Dong, Q. Z. Li, and Y. M. Chai, "Carbon–based transition metal sulfides/selenides nanostructures for electrocatalytic water splitting," *Journal of Alloys and Compounds*, vol. 852, article 156810, 2021.

[48] T. T. Yang, T. L. Tan, and W. A. Saidi, "High activity toward the hydrogen evolution reaction on the edges of MoS_2-supported platinum nanoclusters using cluster expansion and electrochemical modeling," *Chemistry of Materials*, vol. 32, no. 3, pp. 1315–1321, 2020.

[49] L. Mei, X. Gao, Z. Gao et al., "Size-selective synthesis of platinum nanoparticles on transition-metal dichalcogenides for the hydrogen evolution reaction," *Chemical Communications*, vol. 57, no. 23, pp. 2879–2882, 2021.

[50] S. Li, Q. Zhou, G. Yu et al., "Ultra-low cobalt loading on N-doped carbon nanosheets by polymer pyrolysis strategy for efficient electrocatalytic hydrogen evolution," *Applied Surface Science*, vol. 518, article 146239, 2020.

[51] Y. Wang, S. Wang, R. Li et al., "A simple strategy for tridoped porous carbon nanosheet as superior electrocatalyst for bifunctional oxygen reduction and hydrogen evolution reactions," *Carbon*, vol. 162, pp. 586–594, 2020.

[52] Z. Xing, Q. Liu, A. M. Asiri, and X. Sun, "High-efficiency electrochemical hydrogen evolution catalyzed by tungsten phosphide submicroparticles," *ACS Catalysis*, vol. 5, no. 1, pp. 145–149, 2015.